Sensors & Actuators: B. Chemical 345 (2021) 130374

Contents lists available at ScienceDirect

Sensors and Actuators: B. Chemical

journal homepage: www.elsevier.com/locate/snb

Antiresonant hollow core fiber-assisted photothermal spectroscopy of nitric oxide at 5.26 μm with parts-per-billion sensitivity

Karol Krzempek [a,*], Piotr Jaworski [a], Paweł Kozioł [a], Walter Belardi [b]

[a] Laser & Fiber Electronics Group, Faculty of Electronics, Wroclaw University of Science and Technology, 50-370, Wroclaw, Poland
[b] Université de Lille, CNRS, UMR 8523, PhLAM, Physique des Lasers, Atomes et Molécules, F-59000, Lille, France

ARTICLE INFO

Keywords:
Laser spectroscopy
Photothermal gas detection
Antiresonant hollow-core fibers

ABSTRACT

Laser-based gas sensors are undergoing constant and rapid development due to their usability in numerous applications focused on e.g. monitoring of greenhouse gases concentration, safety in harsh environments or medicine. Amongst many types of such sensors, gas detectors employing the photoacoustic or photothermal effect are characterized by an exceptional capability of delivering high selectivity combined with superb signal-to-noise ratio (SNR). In this work, we demonstrate a novel, compact and sensitive nitric oxide (NO) sensor targeting its strong transition near 5.26 μm by combining the photothermal interferometry (PTI) technique and a gas absorption cell based on a self-fabricated antiresonant hollow-core fiber (ARHCF). Having only a 25 cm long interaction length, the sensor reached a minimum detection limit (MDL) of 11 ppbv (parts per billion by volume) for an integration time of 144 s. Proper design of the ARHCF utilized as the gas cell enabled combining a mid-infrared (mid-IR) pump laser to induce the refractive index modulation and a Fabry-Perot interferometer-based readout of the photothermal effect with a near-infrared probe laser. The presented results document the first experimental attempt to detect gas molecules having transitions beyond 4.5 μm in an ARHCF-aided photothermal detection scheme.

1. Introduction

Laser spectroscopy of gases has proven to provide selectivity, sensitivity and in vivo capabilities at the level not achievable in any other type of gas sensors. The superb performance of laser-based gas sensors experiences unstoppable enhancement as a direct result of the development of photodetectors, multipass cells, signal processing techniques and compact, low-power mid-IR laser sources - quantum cascade lasers (QCL) and interband cascade lasers (ICL), which allow accessing the strongest absorption lines of numerous molecules. This paved the way towards numerous out-of-lab applications in detecting the composition of liquids, solids and gases in a nondestructive way [1]. One of the crucial applications of laser spectroscopy is the measurement of the concentration of gases hazardous to both life and environment, e.g. NO. NO gas is used in industrial chemistry and is a byproduct of combustion systems. Due to its high toxicity and harmful influence on the environment (acid rains and ozone depletion), NO leaks or its elevated concentration in the workspace are high risk factors, which require constant monitoring (NO LD50 dose ~300 ppm) [2]. Numerous well-established approaches to NO detection have been developed up to date, however laser-based spectroscopy remains a method delivering unprecedented selectiveness, fast response times, record lifetimes and long-term stability [3]. In the literature, one can find several dissimilar approaches to the problem of detecting NO molecules with the aid of laser spectroscopy. Most of them rely on using multipass absorption cells to achieve the desired laser-gas interaction length required for sensitive detection, and target the strong absorption lines located near ~5.2 μm [4]. However, purely absorption-based laser spectroscopy techniques have several drawbacks resulting from the relatively weak immunity to external factors, the presence of optical fringes, etc. that significantly limit their SNR characteristic, hence negatively influencing the detection capability. Therefore, new methods for omitting the aforementioned problems have to be developed and implemented into the laser-based gas sensor configurations. Two recent decades have brought a tremendous improvement in photoacoustic spectroscopy (PAS) and photothermal spectroscopy (PTS) gas detection techniques, which have unique advantages over traditional, absorption-based laser gas sensors – high sensitivity with short interaction paths, wide dynamic ranges, and zero background signal [5–8]. In PAS and PTS, the gas sample under test is excited by a light source – *pump* (e.g. a laser

* Corresponding author.
E-mail address: karol.krzempek@pwr.edu.pl (K. Krzempek).

https://doi.org/10.1016/j.snb.2021.130374
Received 23 April 2021; Received in revised form 8 June 2021; Accepted 26 June 2021
Available online 29 June 2021

targeting one of the absorption lines), which results in localized heating of the molecules (along the *pump* beam). If the *pump* beam is modulated with a sine or square wave or pulsed, the periodic temperature gradient generates an acoustic wave. In PAS, the acoustic wave can be effectively detected using microphones, quartz tuning forks or cantilevers [9]. The PTS approach however focuses on probing the varying refractive index (RI), which results from the excited (heated) gas sample. Common techniques use Fabry-Perot interferometers (FPI) [10] or Mach-Zehnder interferometers (MZI) [11] to retrieve spectroscopic signals and obtain the required sensitivity of the sensor. In PAS and PTS, the amplitude of the generated effect is proportional to the optical intensity of the *pump* laser radiation and the concentration of the gas sample [12]. The interferometric RI modulation signal retrieval is commonly realized using mature, inexpensive and reliable near-infrared (near-IR) fiber components (e.g. working in the 1550 nm wavelength region) – called the *probe*. Recent years brought a revolutionary innovation in laser spectroscopy, which is a result of combining the PTS technique with hollow-core fibers (HCF). The air core of a HCF enables the guidance of light and can be simultaneously used as a low-volume absorption cell, if filled with the target gas sample. Moreover, in a HCF the *pump* beam can be confined and guided in ten-of-micrometers size mode, which maximizes the power density interacting with the gas molecules. Furthermore, properly designed and fabricated HCFs have the unique possibility of guiding light in several broad, low-loss transmission bands. This enables using mid-IR lasers to target strong absorption lines of gas molecules, at the same time permitting utilizing fiber components to realize the *probe* part of the PTS-based spectroscopic signal retrieval. With correct beam coupling a nearly perfect overlap between the *pump* and the *probe* beams can be achieved, which leads to a significant enhancement of the PTS signal amplitude without the need of using complex, bulk optic-based configurations. This enabled designing miniaturized sensors having superb sensitivity and wide dynamic ranges [10]. The revolution in HCF-based PTS gas sensors is currently gaining momentum with the development of novel types of fibers capable of guiding mid-IR light with low loss, the so-called Antiresonant Hollow-core Fibers (ARHCFs) [13,14]. These fibers solve most drawbacks recognized in the sensors based on the previous designs of HCF, i.e. multimode guidance, small core size and high transmission loss. In ARHCFs, the unique guiding mechanism and structure limits the overlap between the glass capillaries forming the cladding and the laser beam, thus allowing transmitting mid-IR light with low attenuation and in a single transversal mode. This enables accessing the strongest transitions of numerous gas molecules, located beyond 3 μm, which was identified as the most severe limitation of every sensor based on the previous generation fibers. Moreover, the air cores of the ARHCFs have diameters in the range of several tens of micrometers, which simplifies the gas-filling process and reduces the time required to load the fiber-based gas cell with the sample. Mature fiber drawing technology permits manufacturing of fibers in virtually any length, making the ARHCF-based PTS sensors an interesting alternative to gas detectors relying on bulky and fragile multipass cells. Despite the tremendous documented advance in PTS sensors, no research experimentally verified the possibility of designing and building a fiber-based sensor capable of targeting gas molecules transitions beyond 4.7 μm.

Here, we report, to our best knowledge, the first demonstration of a fiber-based PTS gas sensor operating at a wavelength beyond 4.7 μm. As a result of the unique configuration, combining the FPI approach and a self-fabricated low-loss ARHCF, the constructed sensor was capable of targeting strong transitions of NO located at 5.26 μm and reached a minimum detection limit of 11 ppbv at 144 s of integration time. The results show the full potential of combining a novel ARHCF with PTI gas detection technique and pave the way towards designing compact, robust and sensitive gas sensors, which do not require expensive mid-IR detectors and optical components to operate.

2. Materials and methods

2.1. Theory

The principle of operation of the sensor relies on the PT effect, which is observable in gases excited by a radiation source - *pump*. The absorbed energy locally heats the gas sample, which results in an RI change occurring along the pathlength of the *pump* laser. The miniscule variations of the RI require precise methods of probing. Here, we use the PTI technique that involves building an FPI cavity around the gas absorption cell (GAC, see subsection 2.2). With a proper sensor design, the *pump* laser can target strong absorption lines of various gases located in the mid-IR wavelength region, while the FPI-based readout of the induced PT effect can be realized using inexpensive, yet reliable fiber components, e.g. designed to operate in the telecom transmission band. This approach has been widely used in PTS gas sensors based on an MZI or a FPI configuration [15–20]. In this experiment, we use 1550 nm fiber technology to probe the phase modulation occurring in the FPI interferometer. By exciting the gas sample inside the FPI, the PT-induced RI change will modulate the phase of the *probe* light circulating in the cavity. The intensity of the phase change Δθ can be expressed as follows [21]:

$$\Delta\varnothing = k\alpha\left(\lambda_{pump}\right)CLP_{pump} \tag{1}$$

where C is the gas concentration, $\alpha\left(\lambda_{pump}\right)$ is the absorption coefficient at the *pump* wavelength, L is the length of the FPI, P_{pump} is the *pump* power of the laser inducing the RI modulation. The k depends on the gas parameters, modulation frequency of the *pump* light and the guidance parameters of the fiber used as the gas cell (i.e. mode field diameter for *pump* and *probe*, beam overlap, etc.). The amplitude of the phase modulation is linearly dependent on the *pump* power, gas molecules concentration and the length of the FPI, thus can be conveniently used to determine the concentration of the target gas. The *probe* phase modulation will result in a variation of the signal amplitude exiting the FPI. Fig. 1(a) shows the measured and simulated FPI signals as a function of wavelength of the *probe* laser.

The measured free spectral range (λ_{FSR}) of the constructed FPI is 4.8 pm, which closely matches the value calculated based on $\lambda_{FSR}=\lambda^2/2\,L$. According to the measured signal, the minimum transmission of the FPI is equal to $T_{MIN} \approx 0.706$, which allows to calculate the Finesse (F) of the FPI, as follows: $F = T_{MIN}{}^{-1}\text{-}1 = 0.416$. The simulated transmission was calculated based on the following formula [23]:

$$T = \frac{1}{1 + F\cdot\sin\left(\frac{2\pi nd}{\lambda}\right)^2} \tag{2}$$

where T is the FPI transmission and n is the refractive index of the FPI.

2.2. Design of the absorption cell

The GAC design used in the experiment is depicted in detail in Fig. 2. The main part of the sensor consists of a self-fabricated 25 cm long ARHCF. The fiber was drawn down from a borosilicate glass preform to the final structure consisting of 8 nontouching circular capillaries forming the fiber cladding and the hollow air core with a diameter of 122 μm. The unique structure and light guidance mechanism of the fiber allowed obtaining a 1.6 μm wide, low-loss transmission band in the mid-IR spectral window, attenuation at the level of ~ 4 dB/m at 5.26 μm and single-mode characteristic [24]. In comparison to previously published experimental work [21,23], we decided to use a novel method of filling the fiber. Instead of using fixed ceramic ferules to which the fibers are glued, we micro-machined a series of 15 micro-channels in the center of the ARHCF using a femtosecond 1030 nm laser [25]. The fabricated micro-channels provide direct access to the air core of the fiber through

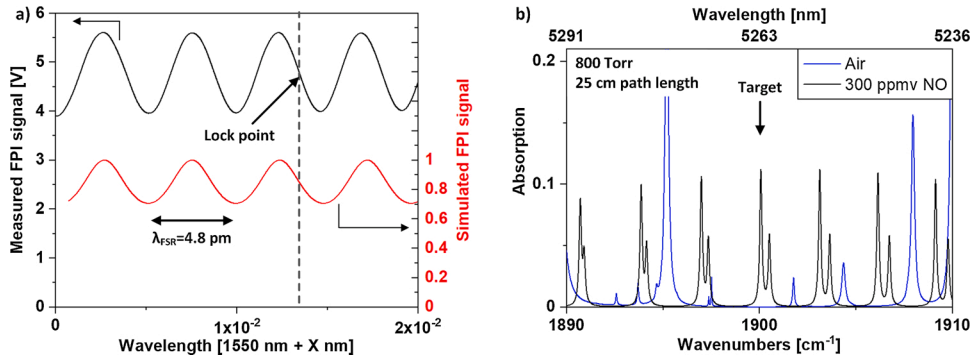

Fig. 1. (a) Measured (black) and simulated (red) FPI signals plotted as a function of wavelength of the probe laser. The dashed line shows the quadrature lock point used during experiments. (b) Absorption spectra for ambient air and 300 ppm by volume (ppmv) of NO diluted in N_2, simulated based on HITRAN database for 800 Torr and a 25 cm long pathlength [22]. The NO transition used in the experiments is highlighted with an arrow.

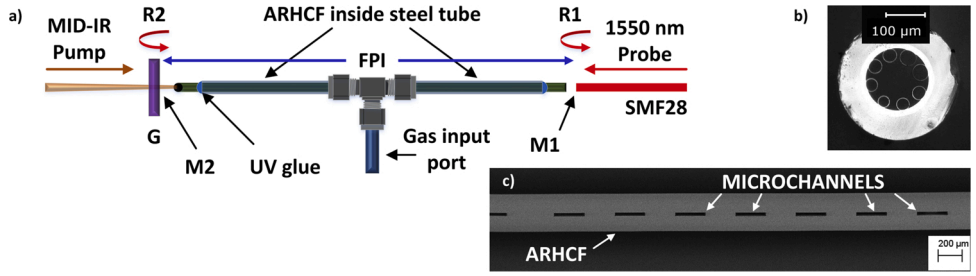

Fig. 2. (a) Schematic of the ARHCF-based gas cell. FPI – arrows show the Fabry-Perot interferometer cavity boundaries, ARHCF – antiresonant hollow core fiber, M1; M2 – mirror surfaces for the FPI, R1;R2 – reflection points of the probe beam, G – germanium wedge. (b) Microscope image of the cross section of the ARHCF used in the experiment. (c) Scanning Electron Micrograph (SEM) image of the micro-channels fabricated in the middle of the ARHCF.

the gaps between the capillaries forming the cladding. Fig. 2 shows the machined micro-channels with a total cross section equal to 0.0675 mm^2, which is twice the cross-section of the ARHCF air core. The fiber was then inserted and glued into a 1/16" diameter SWAGELOK® tee with two 11 cm long steel tubes extruding from each side of the union, using a UV-curable glue, leaving only a ~1 cm long bare unprotected fiber at both ends. Both fiber end facets were carefully cleaved with a ceramic blade. The steel tee and tubes served as a sturdy anchor point for fixing the sensor onto the optical table, and simultaneously the third port of the tee allowed for simple exchange of the gas sample under test, either by applying slight overpressure or under-pressure to the port. Since the micro-channels were fabricated in the middle of the fiber, only a single gas port was required to maintain uniform gas exchange along the entire length of the ARHCF-based gas cell. In the proposed sensor configuration, the readout of the PTS signal relies on an FPI, which probes the induced RI modulation. Two reflecting surfaces (R1 and R2 in Fig. 2) are used to produce the interference pattern. The first reflection is achieved from the flat, 90° cleaved SMF28 fiber (M1), which is delivering the *probe* radiation (1.55 µm wavelength) to the FPI and simultaneously gathering the back-reflected light. Due to the difference in the refractive indices (air to solid core of the fiber), the reflection is ~4%. The second reflecting surface (M2) is realized at a germanium (G) wedge (antireflection coated for wavelengths 1.9 µm – 6 µm), which has a 64.8 % reflectance at the *probe* wavelength and provides a 95.5 % transmission at the *pump* wavelength - 5.26 µm. The SMF28 fiber and the germanium wedge were positioned using 5-axis micro-mechanical stages to achieve several tens of micrometers gaps between the end of the ARHCF and the reflecting surfaces together with a proper angular alignment. In [21,23] the Authors used ceramic ferules to mechanically splice the ARHCF-based gas cell to a mid-IR fiber at one end and to an SMF28 fiber on the other end. Although this method should in principle provide better results in terms of the stability of the set-up FPI, in fact, it resembles only a slightly less complex design then the one proposed in this manuscript. The previously published configurations required a set of bulk-optics components to couple the *pump* laser radiation into the mid-IR single-mode fiber. This approach introduced more than 6 dB of loss to the optical power coupled into the ARHCF, which directly translated to a 4x lower PT signal registered by the sensor. In our approach, the mid-IR *pump* radiation is coupled directly to the gas cell using a single lens, thus closely matching the MFD and numerical aperture (NA) of the ARHCF, reaching a 76 % coupling efficiency (here defined as the ratio of the optical power registered at the fiber output to the coupled optical power).

2.3. Experimental setup

The experimental setup of the sensor is depicted in Fig. 3. NO has been selected as the target gas to experimentally verify the suitability of the proposed PTI-based gas sensor for detecting gaseous substances having absorption lines at wavelengths beyond 5 µm. NO has several strong rotational transitions in the vicinity of 5.2 µm, which are free from interference from water vapor (H_2O) and other gases usually present in ambient air. The HITRAN-based [22] simulation of the absorption spectrum of NO and ambient air is depicted in Fig. 1(b). The strong peaks in the ambient air simulation (blue plot) are related to the water (H_2O) absorption lines present in in that spectral region. To excite gas molecules we have used a linearly polarized QCL (Thorlabs, QD5500CM1), which could be temperature tuned to 11.8 °C to access the R6.5 transition of NO located at 1900.09 cm^{-1}. The emission of the QCL was collimated and subsequently focused using a plano-convex calcium fluoride (CaF_2) lens with a focal length of 75 mm. The beam was directed through a germanium wedge and aligned with the cleaved end of the ARHCF in the gas cell. Carefully selected light coupling conditions into the ARHCF resulted in 78 mW of mid-IR radiation measured at the output of the ARHCF, yielding a coupling efficiency of 76 %

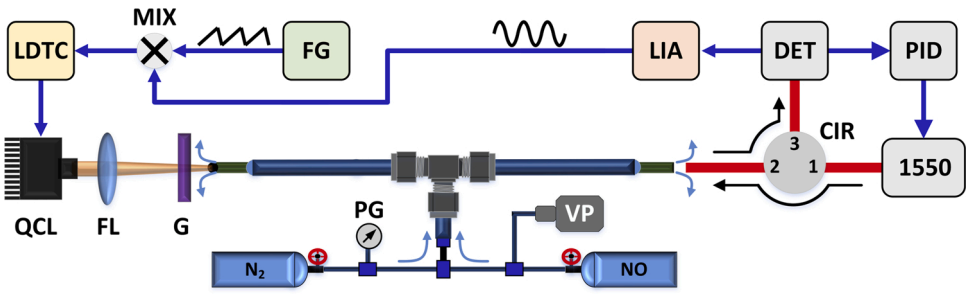

Fig. 3. Experimental setup of the sensor. QCL – quantum cascade laser, LDTC – laser driver with temperature controller, MIX – frequency mixer, FL – focusing lens, G – germanium wedge, FG – function generator, LIA – lock-in amplifier, DET – photodetector, PID – proportional-integral-derivative controller, CIR – fiber circulator, 1550 – 1550 nm laser, PG – pressure gauge, VP – vacuum pump.

The QCL laser was controlled by a temperature and current controller (Thorlabs, ITC4002QCL), which enables external modulation of the current setpoint. This feature was used to employ the Wavelength Modulation Spectroscopy (WMS) technique, which allows obtaining higher SNRs of the registered absorption signal [26]. A sinusoidal modulation of the QCL wavelength at frequency $f_0 = 2.7$ kHz was used (details in subsection 3.1). For registering full 2f WMS scans, we have used an arbitrary waveform generator (FG, Tektronix, AFG3102C) to produce a slow (60 s) saw-tooth ramp, which was superimposed onto the sine-wave modulation signal controlling the current setpoint of the QCL laser. The *probe* laser source was a distributed feedback (DFB) diode laser (Avanex, A1905LMI) with a center wavelength of 1550 nm and an output power of 10 mW, mounted in a current and temperature controller with the capability of external modulation of the current setpoint via the voltage applied to the modulation input (Thorlabs, CLD1015). Its optical power was amplified in a custom-built erbium doped fiber amplifier (EDFA) to 60 mW and delivered through a fiber circulator (CIR) and an SMF28 fiber to the ARHCF gas cell via butt coupling method. The optical power reflected from the FPI was collected by the same fiber and redirected to port 3 of the CIR. The power of the *probe* light at port 3 of the CIR was ~240 μW at the peak reflection of the FPI, which was boosted to 2 mW in the second EDFA, directly before the photodiode (DET) (Thorlabs, PDA10DT-EC). The EDFAs were not included in the schematic in Fig. 3 due to clarity reasons. The voltage signal generated by the DET was delivered to a lock-in amplifier (LIA) (Zurich Instruments, MFLI), which enables analyzing the signal at the second harmonic of the QCL modulation frequency – $2xf_0$. Note that the LIA was also generating the sinewave modulation required for the WMS-based detection. The gas delivery infrastructure was based on the SWAGELOK® components and was equipped with a pressure gauge (PG, MKS, 902B), which ensured that stable and reproducible values of pressure were used during the experiments. The vacuum pump (VP, ILMVAC, 412722) allowed for purging the gas sensor with ambient air, if necessary.

2.4. FPI stabilization loop

Due to the fact that the sensor relies on detecting miniscule variations of the *probe* light phase, a proper method of active stabilization of the FPI cavity is required to achieve satisfactory long-term sensor stability. This can be done by controlling the physical length of the FPI cavity, e.g. by mounting one of the mirrors on a piezo-ceramic transducer (PZT). This approach requires special mounts for the mirrors, high voltage driving electronics and has a limited frequency response due to the weight of the parts moved by the PZT element. Here, the stabilization relies on controlling the optical frequency of the *probe* laser beam entering the FPI. The low-frequency drift of the FPI can be easily compensated by applying the error signal to the modulation input of the *probe* laser driver. Moreover, an active stabilization of the FPI is required to ensure that the FPI is always working in the quadrature point of the interference pattern, even during gas pressure cycling. By actively locking the probe laser wavelength to the FPI quadrature point the sensor is capable of delivering a linear conversion of the induced RI modulation to a voltage signal observed by the photodiode monitoring the output of the interferometer. The feedback loop uses a proportional-integral-derivative controller (PID) (Vescent, D2-125), which monitors the voltage signal delivered by the photodiode. Here, the quadrature point corresponded to a DC voltage of 4.78 V and any drift of the amplitude is corrected by the PID controller by an appropriate voltage signal applied to the modulation input of the *probe* laser driver, hence providing a lock of the *probe* laser wavelength to the FPI cavity transmission. Note that the PID controller error signal input low-pass filter corner was set to 400 Hz, limiting the influence of the control loop on the registered PTI signal. Experimental results showing the performance of the stabilization method are depicted in Fig. 4. During the measurement, the *pump* laser was tuned to the center of the target NO transition located at 1900.1 cm^{-1}.

Fig. 4(a) shows the effect of opening the NO gas valve on the FPI cavity length. Due to the diffusion, the gas concentration in the sensor decreases over time if the gas sample is not constantly flowing through the sensor (note, the lower signal amplitude). Opening the NO valve a t = 0 resulted in filling the entire sensor volume with the gas sample (300 ppmv NO in N_2). However, with no active locking of the cavity, the recorded 2f WMS signal will oscillate until an equilibrium pressure in the GAC is reached. In Fig. 4(b) the FPI signal was registered for 5 min without the PID-based active stabilization and after engaging the PID control loop at t = 0. With no stabilization, the FPI signal experienced a significant drift, which is mostly due to the thermal-related micro-movement of the 5-axis stages used in the experiment to position the reflective surfaces of the interferometer. The experimental results clearly show that active stabilization of the FPI is mandatory for proper operation of the gas sensors relying on this particular method of PT signal readout, and that the proposed active stabilization method is sufficient to maintain quadrature operation of the FPI. Note that the PID controller allowed setting both the proportional, integral and derivative terms of the stabilization loop and the input signal filtering parameters. This ensured that the stabilization approach used in the experiment had a negligible effect on the amplitude of the registered signal. Based on the experimental data, we conclude that the stabilization of the FPI at the quadrature point via *probe* wavelength control is noncomplex, requires no high-voltage piezo transducer-based mechanism of controlling the mirror separation and assures stability of the sensor.

3. Results

3.1. WMS parameters optimization

The sinusoidal voltage signal required for the WMS detection technique was generated directly by the LIA used in the experiments. The signal was applied to the modulation input of the LDTC controlling the

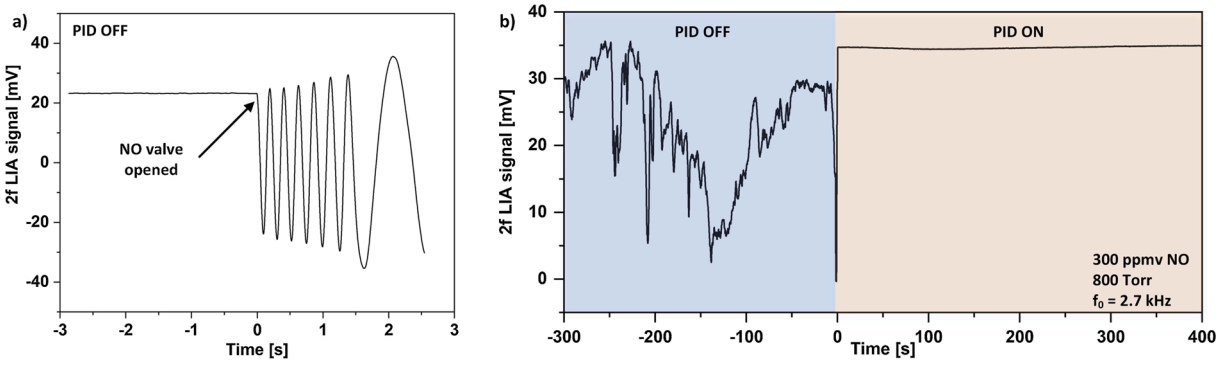

Fig. 4. (a) FPI signal modulation resulting from elongation of the cavity due to a pressure change at t = 0, registered with PID stabilization OFF. (b) Slow drift of the FPI cavity registered for an unlocked PID (blue region) and after locking the probe laser wavelength to the FPI cavity quadrature point at t = 0 (orange region). The signal was measured for 300 ppmv of NO flowing through the sensor at 800 Torr.

current setpoint of the QCL laser. The LIA has an option to sweep the parameters of the generated signal (amplitude and frequency), which was necessary to evaluate the optimal parameters for the WMS-based signal retrieval. In PAS and PTS, the amplitude of the registered signal is inversely proportional to the frequency at which the *pump* laser is modulated [12]. This is due to the fact that the excited molecules have a limited time, during which the induced localized heat is retransferred to the surroundings, mainly via the collision energy transfer [14]. Some researchers choose to use low modulation frequencies, as this produces maximum PT signal, however, 1/f noise is dominant here, limiting the performance of the sensor. Therefore, the proper approach for optimizing the sinewave modulation parameter in gas sensors relying on the PT effect requires determining the tradeoff between the maximum registered PT signal and the amount of noise picked-up by the sensor in the low-frequency range – namely, the SNR for each given modulation frequency setpoint. Fig. 5 sums-up our experimental results on optimizing this parameter.

The measurement of this parameter was performed by sweeping the frequency of the sinewave modulation of the *pump* laser f_0 in the range between 100 Hz and 200 kHz. The LIA was capable of producing a wavelength sweep of f_0 with a density of 10,000 points/range, which allowed plotting the graphs with sufficient setpoint resolution. The black plot in Fig. 5(a) shows the noise density spectrum of the constructed FPI as a function of the sinewave modulation frequency. The drop of noise density registered for frequencies below 300 Hz is directly connected with the low-pass edge filter setting of the PID loop, which was set to compensate the thermal drift of the FPI and low-frequency mechanical and acoustic noise affecting the cavity. The red plot shows the noise density of the detector used in the experiment. This plot indicates the ultimate noise limit of the constructed PTI gas sensor. In the proposed sensor configuration, the overall noise was a combined effect of the FPI stability and the output power stability of the amplifiers used to boost the optical power of the DFB *probe* laser. In its current configuration, the sensor has more than two orders of magnitude margin for further optimization, which would significantly benefit the overall SNR. The peaks in the detector noise spectrum (200 Hz, 12 kHz, etc.) are connected with the power supply noise, which, if necessary, can be omitted with the use of additional filtering or battery-based power supplies. In Fig. 5(b), the 2f LIA signal was measured as a function of the sinewave modulation frequency (black plot). The PID loop dampening of the signal is clearly observable at frequencies <300 Hz. The red plot in Fig. 5(b) shows the SNR of the sensor calculated by point-by-point division of the noise values (black plot Fig. 5(a)) and the 2f LIA signal values. This graph clearly points the sinewave modulation frequency of 2.7 kHz, which yields an optimal SNR. This value was set in each of the following experiments. The second parameter requiring fine-tuning in the WMS detection techniques is the sinewave modulation depth. The LIA used in the experiment allows for performing a continuous scan of the sinewave modulation amplitude generated by the AUX1 output (connected to the modulation input of the *pump* laser driver), which significantly simplified this measurement and allowed registering the response of the sensor with a very high resolution. The results of the measurements are depicted in Fig. 6.

Based on the performed measurements, the optimal modulation

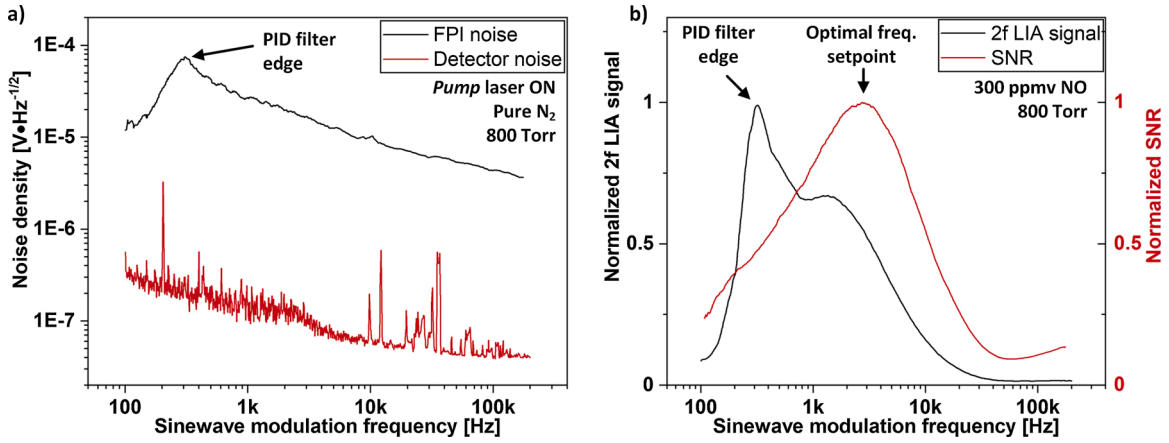

Fig. 5. Pump laser sinewave modulation frequency optimization. (a) Black plot presents the noise density spectrum of the FPI plotted as a function of the sinewave modulation of the pump laser. Red plot shows the noise density spectrum of the detector used in the experiment for monitoring the FPI signal. (b) Black plot presents the normalized 2f LIA signal as a function of the sinewave modulation of the pump laser. Red plot shows the normalized SNR calculated point-by-point based on the FPI noise from black plot in Fig. 5(a). The 2f LIA signal amplitude was measured for 300 ppmv NO at 800 Torr in the sensor.

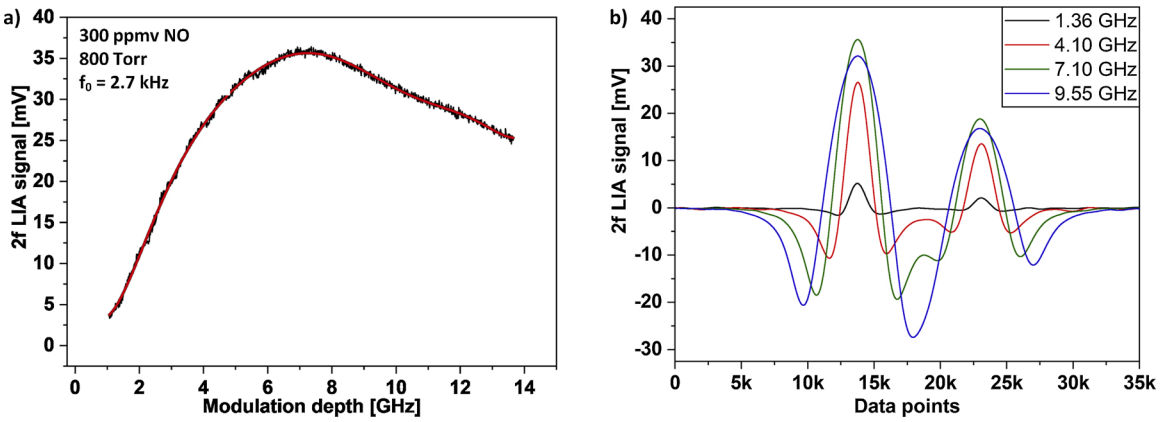

Fig. 6. (a) Sensor response for varying sinewave modulation depth. Red line represents a polynomial fit. (b) full 2f WMS signals registered for the given values of the modulation depth. The measurements were taken for 300 ppmv of NO in the sensor at 800 Torr and $f_0 = 2.7$ kHz.

depth was determined to be 7.1 GHz, at which the maximum amplitude of the registered 2f WMS signal reached 35.9 mV. Fig. 6(b) shows full wavelength scans across the absorption line doublet of NO for several setpoints of the modulation depth value. Note that for higher setpoints of the modulation depth the signals from the individual absorption lines begin to merge significantly.

3.2. Experimental results of NO detection at 5.26 μm

To evaluate the performance of the sensor we have verified its response to varying measurement parameters - the optical power of the *pump* laser and the concentration of the measured NO gas sample. During the measurement the sine-wave modulation was set to $f_0 = 2.7$ kHz with a modulation depth of 7.1 GHz, as evaluated in subsection 3.1. The maximum registered 2f WMS signal is shown in Fig. 7(a) in a full 2f WMS scan.

After optimizing the parameters, the maximum 2f WMS signal amplitude reached 35.9 mV for *a pump* power of 78 mW (measured at the output end-facet of the ARHCF). The registered signal shows no significant background noise and fits with the signal simulated based on HITRAN database and the parameters used in the experiment. The slight offset can be contributed to nonideal current tuning of the QCL laser and residual amplitude modulation [27]. The modulation depth was calculated and expressed in GHz units by transmitting the *pump* laser beam through a 50.8 mm long germanium etalon (Light Machinery, OP-5483) and measuring the amplitude spectrum with a mercury cadmium telluride photodetector (MCT, VIGO, PVI-4TE-5). Fig. 8 shows the experimental results registered for different values of *pump* power.

The optical power coupled into the ARHCF was varied by placing a holographic wire grid polarizer (HWGP, Thorlabs, WP25H-B) in the *pump* beam path (before the CaF_2 lens) and rotating it to achieve the desired power splitting ratio. The pump power was measured by a thermal power sensor (Thorlabs, S401C) directly at the output of the ARHFC, while the gas cell was filled with pure nitrogen (N_2). Maximum 2f WMS signal amplitude at a given measurement point was registered for 300 ppmv of NO in the gas cell and the *pump* laser tuned to the center of the NO transition located at ~1900.1 cm^{-1}. The noise amplitude was measured at each setpoint for 60 s with a LIA TC (time constant) set to 1 s and the gas cell filled with pure N_2. The 2f WMS signal amplitude increases linearly with the pump power, which agrees with Eq. 1. The amplitude of the registered noise remained at a comparable level at each setpoint of the *pump* power, which confirms that the unabsorbed mid-IR *pump* power does not influence the 1550 nm *probe* readout of the FPI signal. Note that the maximum 2f WMS signal reached 30.4 mV due to the insertion loss introduced by the HWGP. In Fig. 9 the 2f WMS signal amplitude registered by the LIA is plotted as a function of varying NO concentration.

The linearity of the sensor response was measured by preparing 7 gas samples containing NO diluted in N_2, using a commercial gas mixer (Environics, 4020). During the measurement, the *pump* laser was tuned to the center of the NO transition located at ~1900.1 cm^{-1} and each plotted measurement point was averaged for 60 s. The measurement confirmed that the registered signal increases approximately linearly with the measured gas concentration, yielding an R-square value of

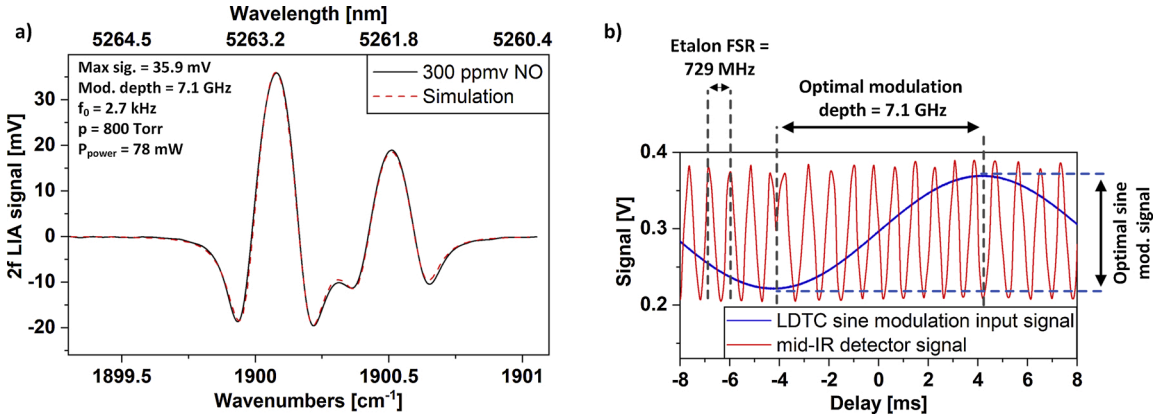

Fig. 7. (a) - black plot shows a full 2f WMS signal registered for the optimized parameters (listed on graph). The red dashed plot shows a simulated signal. b) – experimental determination of the modulation depth. Red trace shows the signal registered with an MCT detector after transmitting the QCL beam through a 50.8 mm long germanium etalon for calibrating the wavelength scan. Blue trace is the sine voltage signal at the LDTC modulation input.

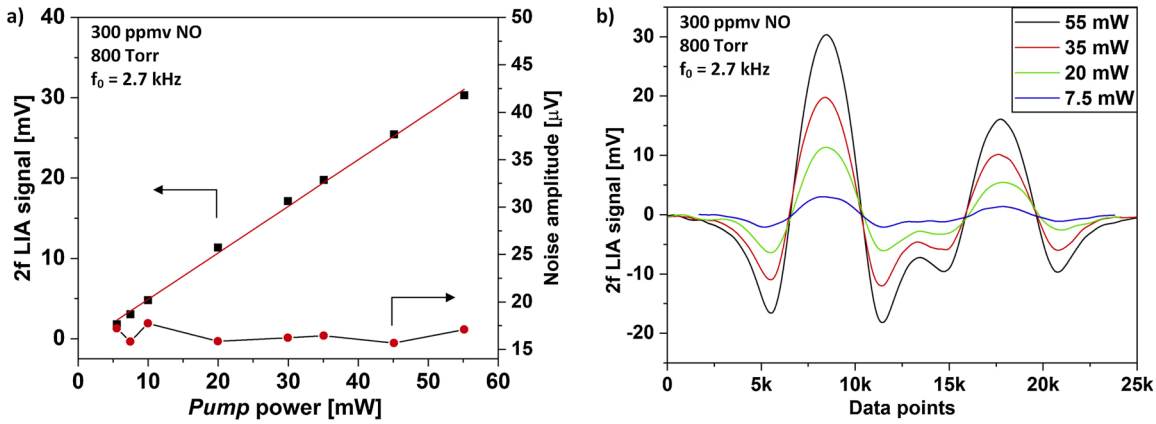

Fig. 8. (a) Maximum 2f LIA signal amplitude measured as a function of pump power coupled into the ARHCF gas cell (black squares). Red solid line represents the signal trend obtained based on Eq. 1. Standard deviation of the noise is plotted with red dots. (b) Full 2f WMS scans of the absorption lines of NO for several setpoints of the pump power.

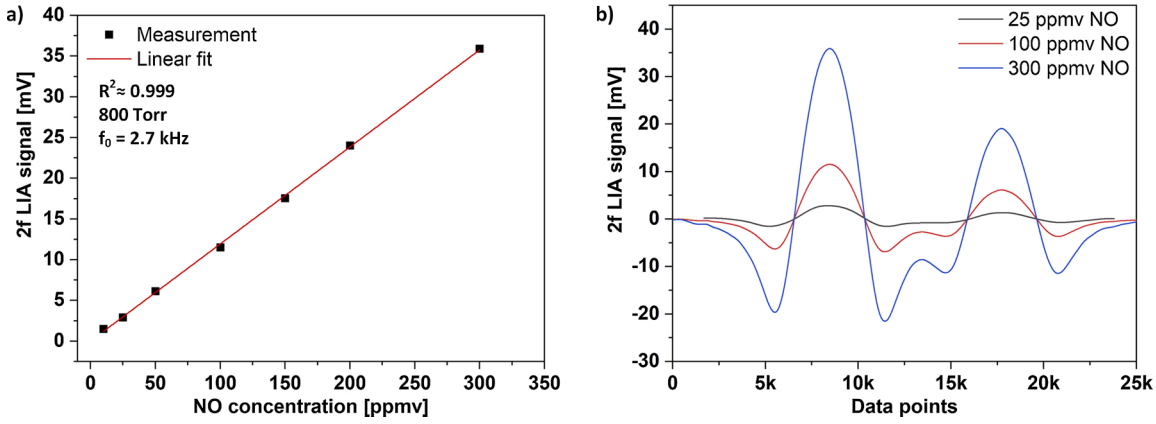

Fig. 9. (a) Maximum amplitude of the registered 2f LIA signal plotted as a function of NO concentration flowing through the gas cell. Red solid line represents a linear fit of the measured values. (b) Full 2f WMS scans of the NO absorption lines registered at 3 different values of NO concentration.

0.9991. The obtained linearity is comparable with previously published experimental work [21,23,28].

3.3. Sensor performance evaluation

In Fig. 10. the performance of the PTI NO sensor was evaluated based on the long-term measurements of the noise, which was compared to the maximum 2f LIA signal achieved for a certified 300 ppmv mixture of NO in N_2. The calculated Allan deviation plots have been expressed both in ppbv and µV, for easier comparison to other PTS sensors having similar configuration. The dashed line in the graph represents the $1/\sqrt{t}$ noise trend, in which the white noise dominates as the source of instability in the sensor. Both calculated Allan deviation plots closely follow the $1/\sqrt{t}$ trend, however the sensor noise deviates from the ideal tendency for

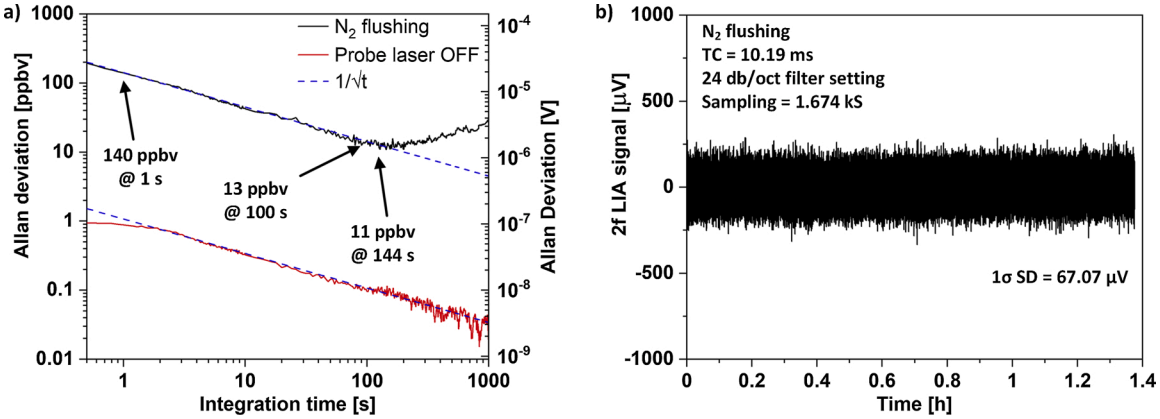

Fig. 10. (a) Allan deviation analysis of the sensor for baseline noise (black trace) and detector shot noise (red trace) expressed in ppbv and in µV units. Dashed blue line represents the $1/\sqrt{t}$ noise trend. Minimum detection limits of the sensor for 1 s, 100 s and 144 s are highlighted in the graph. (b) Time trace of the baseline noise measured for 5000 s for the pump laser turned ON and tuned to the peak of the NO absorption with pure N_2 flowing through the gas cell.

integration times exceeding 144 s, which indicates that different noise sources influence the stability of the measurement. The initial drop registered for the detector shot noise (red trace, *probe* laser OFF) results from different low-pass settings used in this particular measurement (1 s TC) [29]. Ultimately, the sensor reached an MDL equal to 140 ppbv for 1 s, 13 ppbv for 100 s and 11 ppbv for 144 s integration time. This corresponds to a minimum fractional absorption (MFA) equal to 5.41×10^{-5}, 5.0×10^{-6} and 4.19×10^{-6}, for 1 s, 100 s and 144 s integration times, respectively. The measured shot noise of the detector used as the *probe* readout is two orders of magnitude lower, compared to the values calculated for the sensor with the *probe* laser turned ON and flowing N_2. This shows that although obtaining a superior detectivity, when compared to other sensors [17,18,23,28], there is still room for further improvement.

3.4. NNEA calculation

For laser-based gas sensors relying on the PAS, QEPAS (quartz enhanced photoacoustic spectroscopy) or PT detection methods a common unit of performance has been introduced, allowing for comparison between dissimilar configurations – namely the Normalized Noise Equivalent Absorption (NNEA) (W cm^{-1} Hz$^{-1/2}$). It can be determined using the following equation [9]:

$$NNEA = \frac{\alpha P_{pump}}{SNR \sqrt{FBW}} \quad (3)$$

where α (cm^{-1}) can be calculated for the targeted gas absorption line based on the HITRAN database for the given values of wavelength, temperature and gas pressure, P_{pump} is the optical power of the excitation beam, FBW is the filter bandwidth setting used during the measurements taken with the LIA and the SNR is calculated for the given acquisition time. To calculate the NNEA, we have used the following values: $\alpha = 4.76 \times 10^{-3}$ cm^{-1} for 300 ppmv of NO at the 1900.1 cm^{-1} transition, 800 Torr pressure and 25 °C. P_{pump} was equal to 78 mW, the FBW was 78 mHz for 1 s TC set on the LIA (according to the manual) and the SNR for 1 s integration time was 3095, estimated from the data plotted in Figs. 7(a) and 10(a). Based on the given values, the NNEA reached 4.29×10^{-7}. The result is comparable, or superior to sensors having severely more complex configurations [21,23,28,30].

3.5. Gas cell filling time

Sensors relying on hollow-core fiber-based gas absorption cells have to be properly designed to achieve satisfactory gas sample exchange times. Numerous experimental work on PTS sensors was conducted using commercially available hollow-core fibers. Due to a different light guiding mechanism and structure, such fibers introduce severe attenuation for wavelengths > 2 μm, as a result of significant overlap between the guided light and silica cladding [31]. This significantly limits the usability of such sensors, due to the abundance and intensity of the absorption lines in the sub-2 μm wavelength region [1]. The other limiting factor is the small air-core size (usually below 20 μm), which is required to provide light guidance at the wavelength of interest. This results in gas sample exchange times ranging from minutes up to several hours, depending on the fiber type and its length, sensor configuration and methods used to fill the fiber with the target gas mixture [32]. On the other hand, novel ARHFCs can have air cores with tens of micrometers in diameter, which simplifies the gas exchange procedure. To evaluate the gas exchange time in the proposed sensor, an experiment was conducted. Fig. 11 shows the filling time of the gas cell.

Firstly, the gas cell was flushed with pure N_2 and the *pump* laser was tuned to the center of the strong NO transition located at ~1900.1 cm^{-1}. Next, the valves were cycled and the sensor was loaded with 300 ppmv of NO in N_2 at a pressure of 800 Torr. At t = 0 s the registered signal began to increase and reached 90 % of the maximum 2f LIA amplitude after 63 s. The calculated volume of the ARHCF gas cell was 8.12 μL, therefore we estimate the flow to be ~7.7×10^{-3} sccm. Due to the relatively low flow, the gas exchange time is longer when compared to fiber-based sensors relying on absorption-based gas detection techniques [33], where the flow-related noise affects the readout less severely, when compared to the FPI-approach. However, the filling time of our sensor is comparable to other sensors with interferometric signal probing [14]. Based on our observations, the 800 Torr NO pressure provides acceptable filling time, has a negligible effect on the NO absorption line width and is achievable by noncomplex miniature pumps (requirement e.g. for out-of-lab applications).

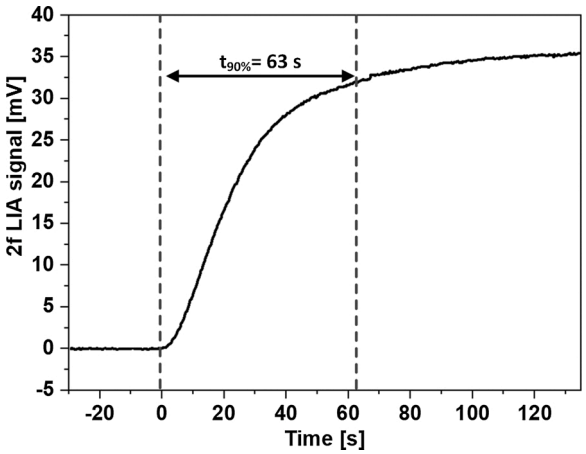

Fig. 11. Measured 2f LIA signal amplitude as a function of time during gas exchange in the ARHCF-based absorption cell.

4. Discussion

PTS has proven to deliver an outstanding result in terms of stability, dynamic range and sensitivity. Dissimilar approaches to retrieve the RI modulation can be adopted, which enables designing state-of-the-art configurations of gas detectors with the aid of novel materials and apparatus. An excellent example is the constant improvement of the ARHCFs, which protrude towards longer wavelengths each year. PTS-based detectors underwent tremendous development with the aid of mid-IR ARHCFs, contributing to their low loss, small air core volumes and the possibility to guide both *pump* and *probe* beams in severely dissimilar spectral bands. With respect to this regard, our investigation was focused on the development of a sensitive and selective PTS-based gas sensor capable of targeting absorption lines of molecules beyond the 5 μm wavelength region, a configuration not yet published. In our experiments we have targeted an NO transition located at ~1900.1 cm^{-1}. The sensor was fully characterized in terms of optimal measurement parameters, its response to varying conditions (*pump* power, gas concentration) and noise characteristics. The constructed sensor reached an MDL of 11 ppbv for a 144 s integration time, which is superior when compared to other sensors relying on multipass cells [15] or utilizing hollow-core fiber-based gas cells [18,34–37] (see Table 1 for full comparison). The self-fabricated ARHCF was used to construct a 25 cm-long gas absorption cell (GAC) with 8.12 μL volume, designed to operate with a pressure close to the ambient. Laser micro-machined microchannels in the middle of the ARHCF ensured convenient filling of the GAC and did not require complex overpressure gas sample delivery infrastructure to achieve satisfactory filling time. The flow of 1.24 sccm was achieved at 800 Torr, yielding a gas exchange time of 63 s. In [21] the Authors were able to mechanically splice the reflective surfaces on both ends of the gas cell, which resulted in less noise pickup of the sensor – standard deviation equal to 19 nV at 410 s, compared to 1.2 μV at 144 s in the proposed configuration. However, the previously published sensor required building a large volume (1.8 L) chamber around

Table 1
Performance of selected gas sensors based on mid-IR HCF-based GACs.

Gas	Type of gas cell	λ	Technique	Cell length	NEA	NNEA	Integration time
Methane [38]	Kagome HCF	3.33 μm	TDLAS	130 cm	4.6×10^{-4}		Not stated
Methane [39]	Kagome HCF	3.33 μm	CLaDS	130 cm	4.0×10^{-4}		1 s
N_2O [40]	HC-NCF	3.60 μm	DAS	120 cm	3.0×10^{-5}		40 s
N_2O [37]	Revolver HCF	4.53 μm	TDLAS	320 cm	1.2×10^{-4}		1 s
N_2O [18]	Capillary fiber	4.46 μm	PTI-MZI	25 cm	5.1×10^{-4}		150 s
Formaldehyde [41]	HC-NCF	3.60 μm	PTI-MZI	120 cm	9.2×10^{-5}		Not stated
CO [30]	Acoustic	4.59 μm	QEPAS	9.4 mm	Not stated	1.6×10^{-7}	1 s
CO [30]	FPI	4.59 μm	PTI-FPI	2 mm	Not stated	3.8×10^{-7}	1 s
Ethane [21]	HC-NCF	3.34 μm	PTI-FPI	14 cm	1.0×10^{-5}		1 s
NO (this work)	ARHCF	5.26 μm	PTI-FPI	25 cm	5.4×10^{-5}	4.29×10^{-7}	1 s
					4.19×10^{-6}		144 s

the fiber-based gas cell to fill it with the measured sample. This undermines the sense of using ARHCFs as a GAC. Moreover, in [14,21] the lower overall noise of the sensor resulted from a combined effect of using mechanical splices and fully passive methods of gas sample exchange via an external gas chamber. By omitting direct flow of gas through the fiber-based gas cell such configuration shows improved long-term stability of the sensor (Allan deviation plots drift from $1/\sqrt{t}$ trend at integration times > 400 s), but simultaneously significantly increases its complexity and gas exchange time, hence the response time of the gas detector. The sensors also relied on constructing the FPI around the gas cell based on Fresnel reflections from flat-cleaved fiber surfaces (R~4%), which yields a lower Finesse, and impacts the 2f LIA signal amplitude registered as a consequence of inducing the PT effect in the gas sample. Furthermore, the solid-core mid-IR fiber used in those experiments as the *pump* beam delivery component has a limited performance in terms of wavelength coverage, which would prevent setting up an experiment targeting absorption lines beyond 5.5 μm. In our sensor the *pump* and *probe* sections of the sensor were separated, simplifying the layout of the sensor and minimizing the number of bulk-optics components required to build the sensor. We have used telecom fiber components to ensure the *probe* section of the sensor is robust, simple to construct and significantly less expensive when compared to the optical components and detectors for the mid-IR. In the literature there are also documented configurations of fiber-based sensors relying on the PTS technique, which achieved superb performance. In work [10], the Authors achieved a noise equivalent absorption of 5.6×10^{-10} cm^{-1} and a very high dynamic range of the sensor – 5.3×10^5. However, the fact that the sensor was constructed based on a fiber designed purely for transmitting wavelengths only in the 1.55 μm telecom band has to be clearly pointed out. Having excellent performance at the *probe* wavelength, such configurations can achieve better overall stability of the PTS signal readout, nevertheless such sensors are limited to sensing only to the sub ~1.6 μm wavelength region, which renders them completely useless for applications requiring targeting strong gas transitions located in the mid-IR wavelength region. The self-fabricated ARHCF used in the experiments is characterized by the unique ability to guide laser radiation both in the telecom band and beyond 5 μm, leading to the superb versatility of the PTS-based gas sensor, reducing its costs and complexity at the level not achievable by the sensors demonstrated up to date.

5. Conclusions

In summary, NO detection with high sensitivity is demonstrated at a record wavelength of 5.26 μm by combining the PTS detection technique with the emerging ARHCF technology, which enables constructing low-volume GACs, ideal for applications in precision spectroscopy. The NNEA reached 4.29×10^{-7}, which due to the proper design of the FPI is in par with the results obtained for significantly more complex configurations, requiring mechanical splicing of the gas cell [21,23], or configurations based on custom FPI [16,28]. The results clearly confirm that with a proper design, PTS sensors relying on ARHCF-based gas cells can outperform detectors relying on traditional detection methods, even at wavelengths recently exclusive for bulk optics-based configurations [33, 42].

Data availability

Data that supports the findings of this study is available from the corresponding author upon reasonable request.

CRediT authorship contribution statement

Karol Krzempek: Conceptualization, Data curation, Formal analysis, Investigation, Methodology, Project administration, Resources, Software, Supervision, Validation, Visualization, Writing - original draft, Writing - review & editing. **Piotr Jaworski:** Funding acquisition, Resources, Writing - review & editing. **Paweł Kozioł:** Resources, Writing - review & editing. **Walter Belardi:** Resources.

Declaration of Competing Interest

The authors report no declarations of interest.

Acknowledgements

This work was supported by the National Science Centre, Poland under "M-ERA.NET 2 Call 2019" [grant number 2019/01/Y/ST7/00088]. We wish to acknowledge Viktoria Hoppe for taking the SEM photography of the micro-channels fabricated in the ARHCF.

References

[1] W. Demtröder, Laser Spectroscopy: Vol. 1: Basic Principles, 4th ed., Springer-Verlag, Berlin Heidelberg, 2008 https://doi.org/10.1007/978-3-540-73418-5.
[2] B. Weinberger, D.L. Laskin, D.E. Heck, J.D. Laskin, The toxicology of inhaled nitric oxide, Toxicol. Sci. 59 (2001) 5–16, https://doi.org/10.1093/toxsci/59.1.5.
[3] Y. Ma, A. Vicet, K. Krzempek, State-of-the-art laser gas sensing technologies, Appl. Sci. 10 (2020) 433, https://doi.org/10.3390/app10020433.
[4] G. Montilla-Bascón, J. Mandon, F.J.M. Harren, L.A.J. Mur, S.M. Cristescu, E. Prats, Quantum cascade lasers-based detection of nitric oxide, in: A. Mengel, C. Lindermayr (Eds.), Nitric Oxide: Methods and Protocols, Springer, New York, NY, 2018, pp. 49–57, https://doi.org/10.1007/978-1-4939-7695-9_5.
[5] Y. Ma, Review of recent advances in QEPAS-based trace gas sensing, Appl. Sci. 8 (2018) 1822, https://doi.org/10.3390/app8101822.
[6] P. Patimisco, G. Scamarcio, F.K. Tittel, V. Spagnolo, Quartz-enhanced photoacoustic spectroscopy: a review, Sensors 14 (2014) 6165–6206, https://doi.org/10.3390/s140406165.
[7] K. Krzempek, A review of photothermal detection techniques for gas sensing applications, Appl. Sci. 9 (2019) 2826, https://doi.org/10.3390/app9142826.
[8] G. Dudzik, K. Krzempek, K. Abramski, G. Wysocki, Solid-state laser intra-cavity photothermal gas sensor, Sens. Actuators B Chem. 328 (2021), 129072, https://doi.org/10.1016/j.snb.2020.129072.
[9] T. Tomberg, M. Vainio, T. Hieta, L. Halonen, Sub-parts-per-trillion level sensitivity in trace gas detection by cantilever-enhanced photo-acoustic spectroscopy, Sci. Rep. 8 (2018), 1848, https://doi.org/10.1038/s41598-018-20087-9.
[10] W. Jin, Y. Cao, F. Yang, H.L. Ho, Ultra-sensitive all-fibre photothermal spectroscopy with large dynamic range, Nat. Commun. 6 (2015), 6767, https://doi.org/10.1038/ncomms7767.

[11] C. Yao, Q. Wang, Y. Lin, W. Jin, L. Xiao, S. Gao, Y. Wang, P. Wang, W. Ren, Photothermal CO detection in a hollow-core negative curvature fiber, Opt. Lett. 44 (2019) 4048–4051, https://doi.org/10.1364/OL.44.004048.
[12] S.E. Bialkowski, N.G.C. Astrath, M.A. Proskurnin, Photothermal Spectroscopy Methods, John Wiley & Sons, 2019.
[13] W. Belardi, F.D. Lucia, F. Poletti, P.J. Sazio, Composite material hollow antiresonant fibers, Opt. Lett. 42 (2017) 2535–2538, https://doi.org/10.1364/OL.42.002535.
[14] H. Bao, H. Bao, Y. Hong, Y. Hong, W. Jin, W. Jin, H.L. Ho, H.L. Ho, C. Wang, C. Wang, S. Gao, Y. Wang, P. Wang, Modeling and performance evaluation of in-line Fabry-Perot photothermal gas sensors with hollow-core optical fibers, Opt. Express 28 (2020) 5423–5435, https://doi.org/10.1364/OE.385670.
[15] K. Krzempek, A. Hudzikowski, A. Głuszek, G. Dudzik, K. Abramski, G. Wysocki, M. Nikodem, Multi-pass cell-assisted photoacoustic/photothermal spectroscopy of gases using quantum cascade laser excitation and heterodyne interferometric signal detection, Appl. Phys. B 124 (2018) 74, https://doi.org/10.1007/s00340-018-6941-x.
[16] J.P. Waclawek, C. Kristament, H. Moser, B. Lendl, Balanced-detection interferometric cavity-assisted photothermal spectroscopy, Opt. Express 27 (2019) 12183–12195, https://doi.org/10.1364/OE.27.012183.
[17] Y. Lin, W. Jin, F. Yang, J. Ma, C. Wang, H.L. Ho, Y. Liu, Pulsed photothermal interferometry for spectroscopic gas detection with hollow-core optical fibre, Sci. Rep. 6 (2016), 39410, https://doi.org/10.1038/srep39410.
[18] Z. Li, Z. Wang, F. Yang, W. Jin, W. Ren, Mid-infrared fiber-optic photothermal interferometry, Opt. Lett. 42 (2017) 3718–3721, https://doi.org/10.1364/OL.42.003718.
[19] K. Krzempek, G. Dudzik, K. Abramski, G. Wysocki, P. Jaworski, M. Nikodem, Heterodyne interferometric signal retrieval in photoacoustic spectroscopy, Opt. Express 26 (2018) 1125–1132, https://doi.org/10.1364/OE.26.001125.
[20] K. Krzempek, G. Dudzik, K. Abramski, Photothermal spectroscopy of CO2 in an intracavity mode-locked fiber laser configuration, Opt. Express 26 (2018) 28861–28871, https://doi.org/10.1364/OE.26.028861.
[21] F. Chen, F. Chen, S. Jiang, W. Jin, W. Jin, H. Bao, H. Bao, H.L. Ho, H.L. Ho, C. Wang, C. Wang, S. Gao, Ethane detection with mid-infrared hollow-core fiber photothermal spectroscopy, Opt. Express 28 (2020) 38115–38126, https://doi.org/10.1364/OE.410927.
[22] L.S. Rothman, I.E. Gordon, A. Barbe, D.C. Benner, P.F. Bernath, M. Birk, V. Boudon, L.R. Brown, A. Campargue, J.-P. Champion, K. Chance, L.H. Coudert, V. Dana, V. M. Devi, S. Fally, J.-M. Flaud, R.R. Gamache, A. Goldman, D. Jacquemart, I. Kleiner, N. Lacome, W.J. Lafferty, J.-Y. Mandin, S.T. Massie, S.N. Mikhailenko, C. E. Miller, N. Moazzen-Ahmadi, O.V. Naumenko, A.V. Nikitin, J. Orphal, V. I. Perevalov, A. Perrin, A. Predoi-Cross, C.P. Rinsland, M. Rotger, M. Šimečková, M. A.H. Smith, K. Sung, S.A. Tashkun, J. Tennyson, R.A. Toth, A.C. Vandaele, J. Vander Auwera, The HITRAN 2008 molecular spectroscopic database, J. Quant. Spectrosc. Radiat. Transf. 110 (2009) 533–572, https://doi.org/10.1016/j.jqsrt.2009.02.013.
[23] F. Yang, Y. Tan, W. Jin, Y. Lin, Y. Qi, H.L. Ho, Hollow-core fiber Fabry–Perot photothermal gas sensor, Opt. Lett. 41 (2016) 3025–3028, https://doi.org/10.1364/OL.41.003025.
[24] W. Belardi, P.J. Sazio, Borosilicate based hollow-core optical fibers, Fibers 7 (2019) 73, https://doi.org/10.3390/fib7080073.
[25] P. Kozioł, P. Jaworski, F. Yu, K. Krzempek, D. Wu, G. Dudzik, M. Liao, K. Abramski, Microdrilling of channels in antiresonant hollow-core fiber using femtosecond laser pulses. Laser Congress 2020 (ASSL, LAC) (2020), Paper JTh2A.3, Optical Society of America, 2020, https://doi.org/10.1364/ASSL.2020.JTh2A.3 p. JTh2A.3.
[26] S. Neethu, R. Verma, S.S. Kamble, J.K. Radhakrishnan, P.P. Krishnapur, V. C. Padaki, Validation of wavelength modulation spectroscopy techniques for oxygen concentration measurement, Sens. Actuators B Chem. 192 (2014) 70–76, https://doi.org/10.1016/j.snb.2013.10.070.
[27] P. Patimisco, A. Sampaolo, Y. Bidaux, A. Bismuto, M. Scott, J. Jiang, A. Muller, J. Faist, F.K. Tittel, V. Spagnolo, Purely wavelength- and amplitude-modulated quartz-enhanced photoacoustic spectroscopy, Opt. Express 24 (2016) 25943–25954, https://doi.org/10.1364/OE.24.025943.
[28] J.P. Waclawek, H. Moser, B. Lendl, Balanced-detection interferometric cavity-assisted photothermal spectroscopy employing an all-fiber-coupled probe laser configuration, Opt. Express 29 (2021) 7794–7808, https://doi.org/10.1364/OE.416536.
[29] P. Werle, Accuracy and precision of laser spectrometers for trace gas sensing in the presence of optical fringes and atmospheric turbulence, Appl. Phys. B 102 (2011) 313–329, https://doi.org/10.1007/s00340-010-4165-9.
[30] D. Pinto, H. Moser, J.P. Waclawek, S. Dello Russo, P. Patimisco, V. Spagnolo, B. Lendl, Parts-per-billion detection of carbon monoxide: a comparison between quartz-enhanced photoacoustic and photothermal spectroscopy, Photoacoustics. 22 (2021), 100244, https://doi.org/10.1016/j.pacs.2021.100244.
[31] Hollow-Core Photonic Crystal Fibers - Glophotonics, (n.d.). https://www.glophotonics.fr/index.php/hollow-core-photonic-crystal-fibers.html (accessed March 6, 2021).
[32] R. Wynne, B. Barabadi, Gas-filling dynamics of a hollow-core photonic bandgap fiber for nonvacuum conditions, Appl. Opt. 54 (2015) 1751–1757, https://doi.org/10.1364/AO.54.001751.
[33] P. Jaworski, K. Krzempek, G. Dudzik, P.J. Sazio, W. Belardi, Nitrous oxide detection at 5.26 μm with a compound glass antiresonant hollow-core optical fiber, Opt. Lett. 45 (2020) 1326–1329, https://doi.org/10.1364/OL.383861.
[34] M. Nikodem, K. Krzempek, G. Dudzik, K. Abramski, Hollow core fiber-assisted absorption spectroscopy of methane at 3.4 μm, Opt. Express 26 (2018) 21843–21848, https://doi.org/10.1364/OE.26.021843.
[35] K. Krzempek, K. Abramski, M. Nikodem, Kagome hollow core fiber-based mid-infrared dispersion spectroscopy of methane at sub-ppm levels, Sensors 19 (2019) 3352, https://doi.org/10.3390/s19153352.
[36] C. Yao, S. Gao, Y. Wang, P. Wang, W. Jin, W. Ren, Silica hollow-core negative curvature fibers enable ultrasensitive mid-infrared absorption spectroscopy, J. Light. Technol. 38 (2020) 2067–2072, https://doi.org/10.1109/JLT.2019.2960804.
[37] M. Nikodem, G. Gomółka, M. Klimczak, D. Pysz, R. Buczyński, R. Buczyński, Demonstration of mid-infrared gas sensing using an anti-resonant hollow core fiber and a quantum cascade laser, Opt. Express 27 (2019) 36350–36357, https://doi.org/10.1364/OE.27.036350.
[38] M. Nikodem, K. Krzempek, G. Dudzik, K. Abramski, Hollow core fiber-assisted absorption spectroscopy of methane at 3.4 μm, Opt. Express 26 (2018) 21843–21848, https://doi.org/10.1364/OE.26.021843.
[39] K. Krzempek, K. Abramski, M. Nikodem, Kagome hollow core fiber-based mid-infrared dispersion spectroscopy of methane at sub-ppm levels, Sensors 19 (2019) 3352, https://doi.org/10.3390/s19153352.
[40] C. Yao, S. Gao, Y. Wang, P. Wang, W. Jin, W. Ren, Silica hollow-core negative curvature fibers enable ultrasensitive mid-infrared absorption spectroscopy, J. Light. Technol. 38 (2020) 2067–2072, https://doi.org/10.1109/JLT.2019.2960804.
[41] C. Yao, S. Gao, Y. Wang, P. Wang, W. Jin, W. Ren, MIR-pump NIR-probe fiber-optic photothermal spectroscopy with background-free first harmonic detection, IEEE Sens. J. 20 (2020) 12709–12715, https://doi.org/10.1109/JSEN.2020.3000795.
[42] D.D. Nelson, J.H. Shorter, J.B. McManus, M.S. Zahniser, Sub-part-per-billion detection of nitric oxide in air using a thermoelectrically cooled mid-infrared quantum cascade laser spectrometer, Appl. Phys. B 75 (2002) 343–350, https://doi.org/10.1007/s00340-002-0979-4.

Dr. Karol Krzempek (KK) obtained his PhD on Nonlinear Frequency Conversion-based Mid-infrared Laser Sources at the Faculty of Electronics at Wroclaw University of Science and Technology (WUST), in 2016. He currently continues his research in this area at the WUST. His main research contributions include design and optimization of CW and pulsed fiber-based laser sources working in the 1 μm, 1.5 μm and 2 μm wavelength regions and subsequent nonlinear mixing of the emission of such coherent sources. Research interests of KK also include sensors relying on photothermal gas detection techniques, as well as efficient use of hollow-core fibers as low-volume gas cells in laser spectroscopy applications. He participated in 13 research grants (4 as Principal Investigator), and is the co-author of 11 national patents. Throughout his academic career, KK received numerous national shoolarships and awards. Recently, KK contributed as a co-editor for MDPI and Forntiers in Physics. He contributed to more than 80 scientific works.

Dr. Piotr Jaworski (PJ) received his PhD in Physics from Heriot-Watt University, Edinburgh, UK in 2015. During his PhD studies he was working on the development of novel antiresonant hollow-core fibers for the delivery of high peak power pulsed laser light in the near-ir and visible spectral range and its application to precision micro-machining. After that he joined in 2015 Lukasiewicz Research Network - PORT Institute (before Wroclaw Research Center EIT+) as a research engineer in Laser Sensing Laboratory. Since than his research work was focused on laser-based gas sensing using both bulk optics-based and hollow-core fibers-based gas spectrometers. In 2018 he became the Head of Laser Sensing Laboratory in PORT. In 2019 he joined the Laser Spectroscopy Group at Wroclaw University of Science and Technology focusing his research on gas sensing using hollow-core microstructured fibers. Piotr Jaworski is an author and co-author of 42 research articles, conference proceedings and conference presentations. He has been a main investigator in 8 research projects and principal investigator in 1 research grant. He also developed two laser-based gas sensing systems for industrial enterprises from Poland.

Dr. Paweł Kozioł (PK) Paweł Kozioł received his PhD in Telecommunication at Wroclaw University of Science and Technology, Poland in 2017. During his PhD studies he was working on the development of the technology of direct laser metallization of the ceramic surface and its application in fabrication of passive metamaterial structures for the microwave and terahertz range. In 2015 he joined the Lukasiewicz Research Network – PORT Institute (prior Wroclaw Research Center EIT+) as a research engineer in Laser Micromachining Laboratory. Since then his research work has been focused on laser modification and material processing using ns, ps lasers for different applications (mainly for industry). In 2019 he joined the Laser Spectroscopy Group at Wroclaw University of Science and Technology focusing his research on integration of sensitive methods of detecting trace concentrations of gases with sensor systems based on low-loss microstructural optical fibers with an air core. Paweł Kozioł is the co-author of 33 research articles, conference proceedings and conference presentations. He was the principal investigator in 1 research grant and the main investigator in 4 research projects.

Dr. Walter Belardi (WB) holds an excellence research chair in Photonics at the University of Lille- CNRS. After several years of cumulated expertise and world-first results on the design, fabrication and use of novel hollow core fibers (in the United Kingdom), he has joined the University of Lille in late 2018. This M-Era.net project would be particular suitable for him and the all scientific research team in Lille to advance further the field of hollow core optical fibers. Dr Belardi has 20 years' experience in the field of specialty optical fibers (SOFs) and, along his career, had the opportunity to develop aspects related to both design, fabrication and the use of SOFs in fields as broad as optical communications, medical diagnostic and surgery, high power optical beam delivery, optical sensing and mid-infrared optics. His combined expertise in both the academic and industrial sector is of particular relevance in a project whose outcome could be of high interest not only for the large research community but also for the European industry.